AGU100 ADVANCING EARTH AND SPACE SCIENCE

Geophysical Research Letters

RESEARCH LETTER
10.1029/2018GL079653

Nocturnal Thermal Fracturing of a Himalayan Debris-Covered Glacier Revealed by Ambient Seismic Noise

Evgeny A. Podolskiy[1,2], Koji Fujita[3], Sojiro Sunako[3], Akane Tsushima[4], and Rijan B. Kayastha[5]

[1]Arctic Research Center, Hokkaido University, Sapporo, Japan, [2]GI-CoRE, Hokkaido University, Sapporo, Japan, [3]Graduate School of Environmental Studies, Nagoya University, Nagoya, Japan, [4]Research Institute for Humanity and Nature, Kyoto, Japan, [5]School of Science, Kathmandu University, Kathmandu, Nepal

Key Points:
- We present the first passive seismic experiment at a debris-covered glacier
- Diurnal air temperature fluctuations influence the broadband seismic noise
- Debris cover protects the glacier ice from thermal stress-induced fracture

Supporting Information:
- Supporting Information S1

Correspondence to:
E. A. Podolskiy,
evgeniy.podolskiy@gmail.com

Citation:
Podolskiy, E. A., Fujita, K., Sunako, S., Tsushima, A., & Kayastha, R. B. (2018). Nocturnal thermal fracturing of a Himalayan debris-covered glacier revealed by ambient seismic noise. *Geophysical Research Letters*, *45*, 9699–9709. https://doi.org/10.1029/2018GL079653

Received 10 JUL 2018
Accepted 24 AUG 2018
Accepted article online 29 AUG 2018
Published online 19 SEP 2018

Abstract Scientifically valuable information can be learned by *listening* to the tiny vibrations emanating from a glacier with seismometers. However, this approach has never been employed to better understand glaciers protected from heat by a debris mantle, despite being common in the Himalayas, one of the most glacierized regions in the world. Here we installed a seismic network at a series of challenging high-altitude sites on a glacier in Nepal. Our results show that the diurnal air temperature modulates the glacial seismic noise. The exposed surface of the glacier experiences thermal contraction when the glacier cools, whereas the areas that are insulated with thick debris do not *suffer* such thermal stress. Thus, the *unprotected* ice surface bursts with seismicity every night due to cracking, which gradually damages and weathers the ice. This is the first time such processes have been observed at relatively warm temperatures and outside of the polar regions.

Plain Language Summary It has been realized that much scientifically valuable information can be learned by *listening* to the tiny vibrations emanating from a glacier with sensitive sensors. However, due to their remoteness and the difficulties in accessing glacial environments, this approach has rarely been employed to better understand these important systems. For example, debris-covered glaciers, which are protected from heat by a debris mantle, remain to be studied despite being common in the Himalayas, one of the most glacierized regions in the world. Here we installed a seismic network at a series of challenging high-altitude sites on a glacier in Nepal. Our results show that the diurnal air temperature modulates the glacial seismic activity. A debris mantle dampens the diurnal amplitude of temperature and thus protects the ice from cyclic mechanical damage, whereas debris-free (exposed) ice experiences intensive near-surface fracturing early in the morning. This implies that the *unprotected* ice surface bursts with seismicity every night due to cracking, which gradually damages and weathers the ice. This is the first time such processes have been observed outside of the polar regions. These findings are in agreement with the personal experiences of climbers who felt and heard loud cracks on high-altitude glaciers at night.

1. Introduction

Technological advances in seismic instrumentation, with the ability to detect micrometer-scale vibrations in media at a high temporal resolution (hundreds of hertz), now provide the opportunity for the characterization and continuous monitoring of subsurface processes that are inaccessible or difficult to observe. These advances have led to recent progress in environmental seismology, which has provided many unique insights into Earth surface processes (Larose et al., 2015). Passive seismic observations are also becoming more commonplace in elucidating cryospheric processes in the field of glaciology (Podolskiy & Walter, 2016) and have already led to several major discoveries, such as glacial earthquakes generated by iceberg calving (Ekström et al., 2003) and the stick-slip motion of ice streams (Wiens et al., 2008).

Himalayan debris-covered glaciers, which occupy about 70% of the glaciated Himalayas (Ojha et al., 2017), are the least-represented type of glaciers in glacier seismology studies (Podolskiy & Walter, 2016). Moreover, the remote areas of the so-called Third Pole, which possesses the largest volume of glacial ice outside of the polar regions and includes the massive glacierized region of the Himalayas and Tibet, remain outside of the mainstream domains of passive cryoseismic studies, such as those on the Antarctic Ice Sheet (Anthony et al., 2015), Greenland outlet glaciers (Podolskiy et al., 2016), Alaskan and Svalbard calving glaciers (Köhler et al., 2012; O'Neel & Pfeffer, 2007), and the mountain glaciers of the European Alps (Roux et al., 2008).

The aims of this study are to provide a wide-scale seismic characterization of the poorly known glaciological environment of a Himalayan debris-covered glacier system and to explore the potential of passive seismic monitoring of Himalayan mountain glaciers. This paper introduces not only the first seismic observations from a debris-covered glacier but also the first Himalayan cryoseismic experiment and the highest glacier-focused seismic network to date (at 4,520–5,550 m above sea level). The results for the first time indicate that cyclic thermal stressing fractures ice, unless the ice is protected by a thick debris mantle.

2. Methods

2.1. Study Site

Trakarding-Trambau Glacier system is located in Rolwaling Valley, Eastern Nepal, near the China border and the neighboring Everest region, which has experienced overall ice mass loss in recent decades (King et al., 2017; Nuimura et al., 2012). The lower part of the glacier is renowned because of its proglacial lake, Tsho Rolpa (Yamada, 1998; Figure 1), which is dammed by a 150-m-high terminal moraine. Tsho Rolpa is one of the largest proglacial lakes in the Himalaya with a total volume of about 90×10^6 m^3 (Rana et al., 2000; Sakai et al., 2000; Shrestha et al., 2011). Its vast size presents the potential risk of a glacial lake outburst flood event, posing a threat to 10,000 people, livestock, hydropower projects, and other infrastructure (Rana et al., 2000; Shrestha et al., 2011).

The Trakarding-Trambau Glacier system is currently separated into two glaciers by a steep rock cliff that is ice free due to increased melting (Figure 1). The lower section consists of Trakarding Glacier, a mostly debris-covered glacier that is situated between approximately 4,520- and 5,030-m elevation, whereas Trambau Glacier is a mostly debris-free glacier that resides above this rock cliff, with a surface elevation ranging from around 5,060 to 6,690 m (Nuimura et al., 2015). Remote sensing studies have identified considerable surface lowering rates across the two glaciers, from about −3 m/year in the debris-free area to −5 m/year in the debris-covered area (King et al., 2017). The debris-covered areas of the glacier system make a significant contribution (55%) to the total runoff due their lower elevations, as inferred by a basin-scale runoff model (Fujita & Sakai, 2014).

A more detailed discussion of the study site can be found in the supporting information (Chikita et al., 1997, 1999; Fujita et al., 2013; Kargel et al., 2016; Sakai et al., 2009).

2.2. Observations

The passive seismic observations of this study formed a component of a comprehensive glaciological campaign focused on the Trakarding-Trambau Glacier system, which was undertaken in the postmonsoon season (17 October to 12 November 2017). The program included meteorological observations from an automatic weather station (AWS), surface elevation mapping from differential global positioning system, ground-penetrating radar measurements of ice thickness, mass balance monitoring with ablation stakes, unmanned aerial vehicle mapping of the area, measurements of debris properties, and shallow ice coring, as well as other activities. The configuration of the seismic network is shown in Figure 1. The stations were positioned on the moraine and the glacier surface between 4,521 and 5,555 m above sea level, and the operational time of the individual stations varied from 2 to 14 days, with a 4-day period of continuous recording at the four main stations (C1–C4). Comprehensive descriptions of the seismic network are provided in the supporting information. Given that each station was deployed in a unique seismic environment, with distinct differences immediately visible in the raw seismic traces (Figure 2), the glaciological conditions at the location of each seismic station are also described in the supporting information.

2.3. Seismic Signal Processing

We followed the standard methodology of McNamara and Buland (2004) to provide a general statistical characterization of the background ambient seismic noise at each seismic station. The fundamental reason for such an analysis is to realistically evaluate the frequency-dependent seismic noise levels by computing probability density functions (PDFs) from a large number of power spectral densities (PSDs). These PDFs allow both the true variation in seismic noise to be estimated and the performance of a given station to be characterized. See the supporting information and McNamara and Buland (2004) for further details on this PSD-based PDF approach.

10.1029/2018GL079653

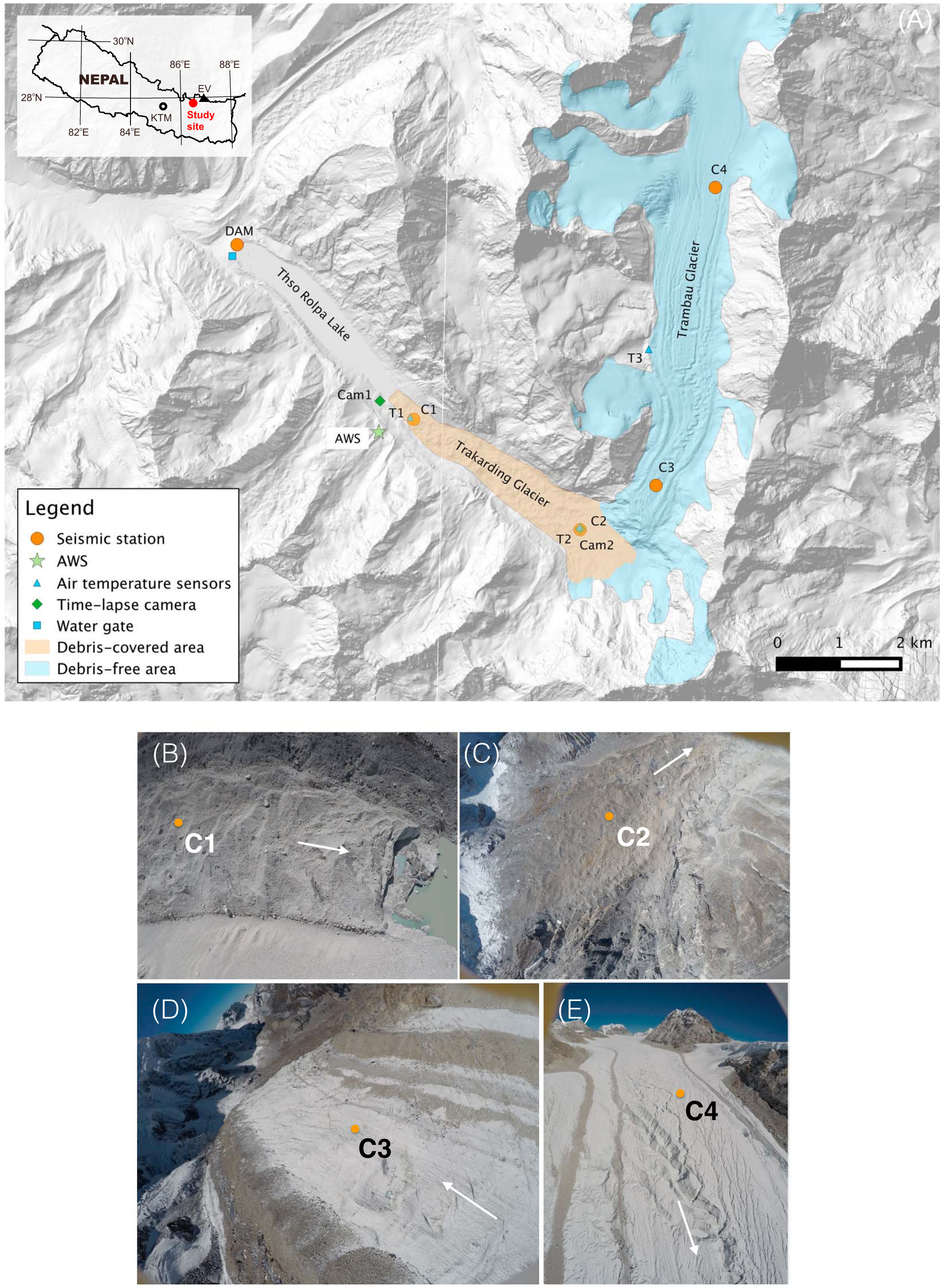

Figure 1. (a) Map showing the locations of the seismometer network and other instruments across the Trakarding-Trambau Glacier system, Nepal Himalaya (27.83° N, 86.52° E), deployed in October–November 2017 (background topography: high-mountain Asia 8-m digital elevation model mosaics). The outline of the glaciers, which marks the 30 October 2000 glacier extent, was adopted from the Glacier Area Mapping for Discharge from the Asian Mountains Glacier Inventory (Nuimura et al., 2015). KTM and EV on the inset map denote Kathmandu and Mount Everest, respectively. (b–e) Oblique aerial unmanned aerial vehicle images over the following seismic station locations: (b) C1, (c) C2, (d) C3, and (e) C4. The arrows correspond to the direction of glacier flow. Images (b) and (c) were taken on 27 October 2017, and (d) and (e) were taken on 7 November 2017 (a courtesy of H. Inoue and Y. Sato). AWS = automatic weather station.

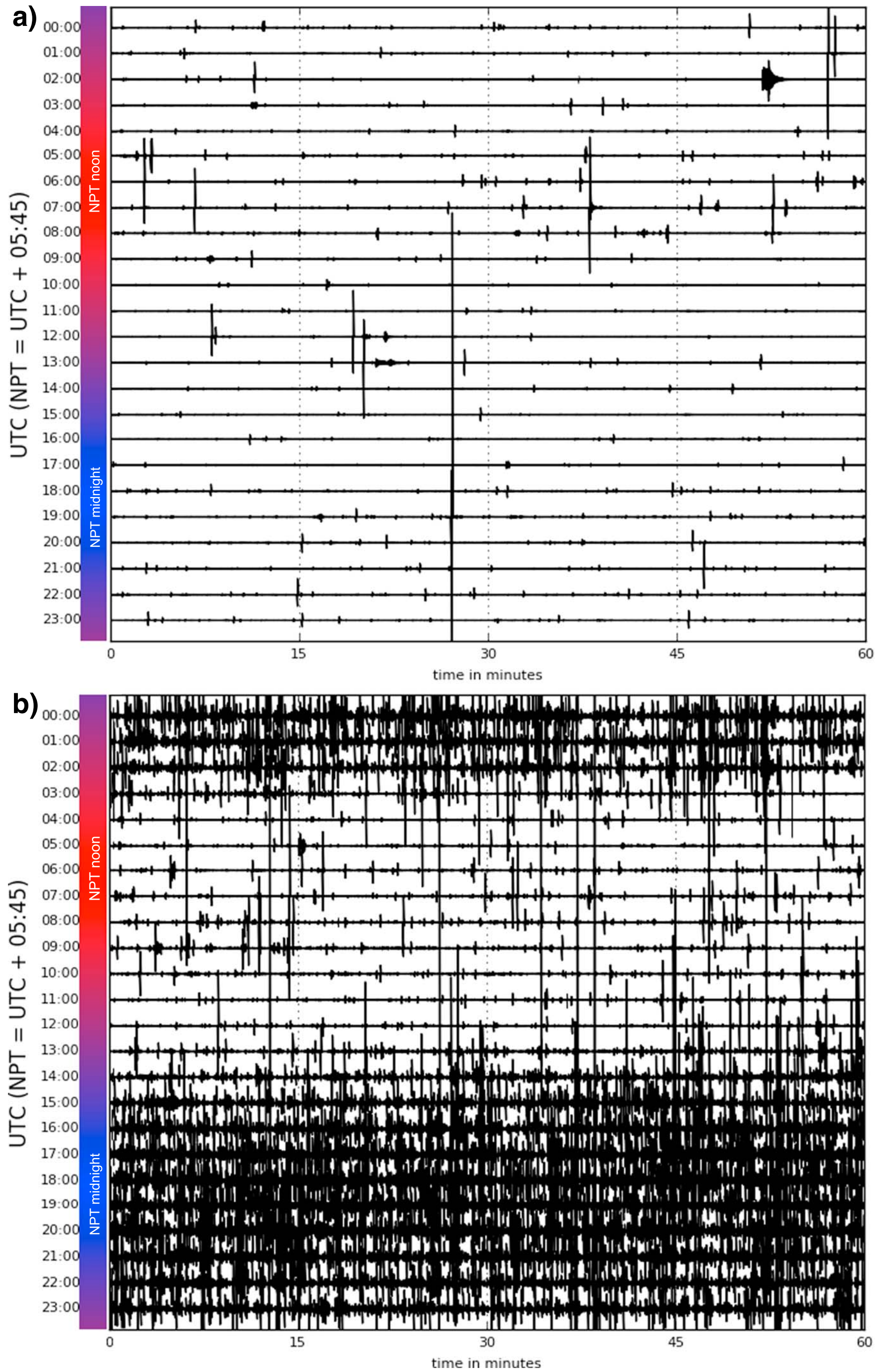

Figure 2. One-day plots of the vertical-component seismograms for 5 November 2017 (bandpass filtered between 4.5 and 30 Hz), at (a) C1 on the debris-covered glacier surface and (b) C4 on the debris-free glacier surface. The color bar schematically indicates the local daytime/nighttime hours. Note the tectonic earthquake around 2:52 a.m. UTC that was recorded by both stations.

To discriminate diurnal characteristics, instead of producing PDFs for daytime and nighttime, which could hide differences between particular days, temporal noise variations were quantified for a series of different frequency bands. We first parsed the instrument-corrected vertical-component time series into 1-min segments and computed their PSDs. Five frequency bands of interest were chosen based on an evaluation of the broadband noise levels in the PSD-PDF results to determine the tremor strength: 0.1 – 1, 1 – 4, 4 – 10, 10 – 30, and 50 – 100 Hz. The power of each time segment was then integrated over the five frequency bands to produce

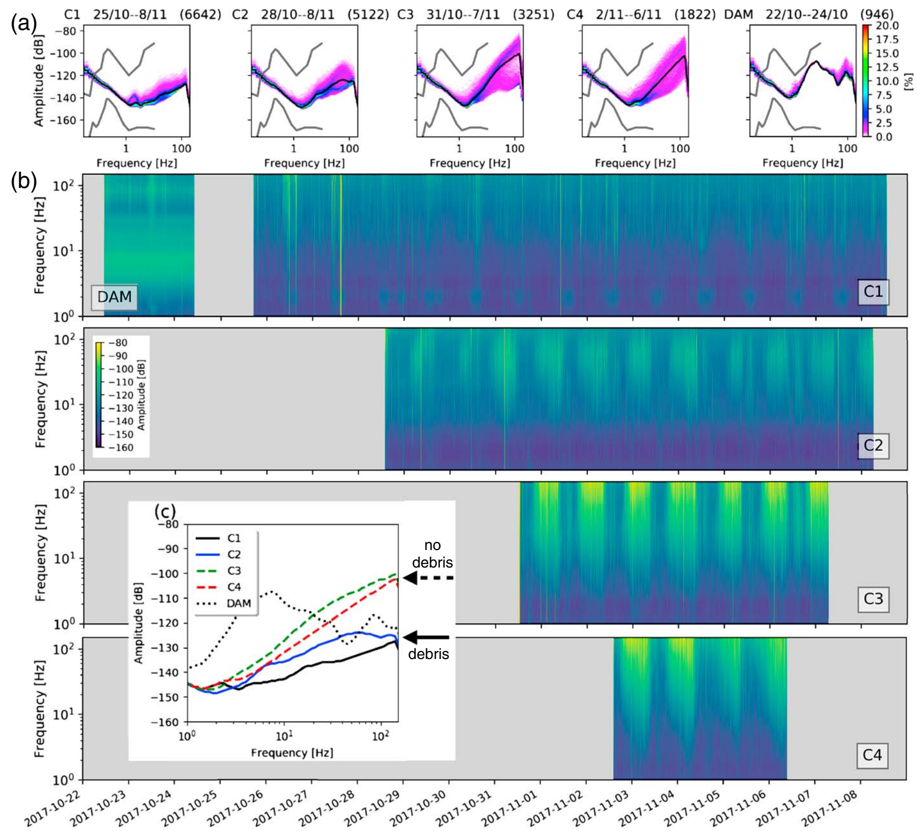

Figure 3. (a) PDFs for each seismic station (amplitude is in $m^2 \cdot s^{-4} \cdot Hz^{-1}$). The corresponding time period (DD/MM) of the PDF analysis and the number of PSDs used for the construction are indicated at the top of each subplot. The standard low and high noise models are shown as gray curves for comparison (McNamara & Buland, 2004). The black curve shows the median power for each PDF distribution. The color bar refers to the probability (%). (b) Temporal evolution of the PSDs for each seismic station. Note that the stations DAM and C1 are plotted at the same subplot. Inset (c): Median power of the broadband PDFs of each station (debris-free sites, C3 and C4, are shown by dashed curves). PDF = probability density function; PSD = power spectral density.

a high-resolution measure of tremor strength. The moving median was computed with a 1-hr window width to smooth the seismic response, and the result at each station was then normalized to yield the relative, nondimensional variations.

3. Results and Discussion

3.1. Noise Maps

Our statistical analysis of ambient noise corresponds to a PDF map of the ambient noise probability level constructed from between 946 and 6,642 PSD sections, depending on the operational time of each seismic station (Figure 3). The final outcome corresponds to a narrow power range of background noise that is specific to each seismic station and includes any transient seismic signals, such as tectonic earthquakes, which are generally low-probability occurrences that do not significantly affect the PSD-PDFs (Anthony et al., 2015; McNamara & Buland, 2004). According to a manual inspection of the traces (e.g., Figure 2) and the National Seismological Centre of Nepal (www.seismonepal.gov.np) analysis, no significant tectonic activity was observed during the campaign period. Our time-lapse cameras also suggested that other transient signals due to snow avalanches or calving were rare events with little effect on the PSD-PDF outcome. We also computed the median power for each frequency bin at each station for a direct comparison of noise between the stations (Figure 3f), noting that the sensitivity tests suggest that these curves are not significantly affected by the number of segments used in the statistics.

The broadband PDFs for all stations show a general increase in ambient noise below 1 Hz, as can be expected due to the globally observable secondary microseisms produced by ocean waves (0.12–0.25 Hz; McNamara & Buland, 2004). However, due to the poor sensitivity of geophones at such low frequencies, this portion of the spectra is smeared with low-frequency artifacts from the instrument correction. Therefore, the PDFs of the stations are nearly identical below 0.5 Hz. Another similarity shared by all stations is above 150 Hz, due to an energy leak near the Nyquist frequency of 200 Hz.

The greatest variability among the PDFs is a clear difference in the seismic response between the on-ice stations (C1 – C4) and the terminal moraine station (DAM; Figure 3). The median power gradually increases with frequency above 2 Hz on the glacier, whereas the corresponding curve on the moraine has a bimodal shape with a primary broad peak around 7 Hz and a secondary peak at 80 Hz. The main mode is condensed into a very narrow amplitude range that suggests little variation in amplitude, while the second mode is smeared. Other smeared signals, possibly pointing to time-varying processes, are located between 0.6 and 2 Hz. Transients due to small tectonic earthquakes, water flow, or wind waves could explain the latter weaker signals, while the main lobes could be associated with structural site effects or wind turbulence around the moraine. The fundamental mode of standing oscillations in the lake basin, known as seiches, would be at significantly longer periods (a few hundreds of seconds according to Merian's formula), whereas wind-induced surface ripples may occur at more relevant frequencies (0.6 to 1.7 Hz; Pore, 1979).

Among the four glacier stations, a key observation is the similarity within each pair of stations from the same type of terrain, which can be separated into the debris-covered glacier stations (C1 and C2) and the debris-free glacier stations (C3 and C4; Figure 3). In particular, C3 and C4 appear similar. The distinct feature of the debris-free PDFs is the very broad and linear increase in amplitude above 4 Hz (Figure 3). Compared with the debris-covered PDFs, this high-frequency content is up to 30 dB larger (e.g., the 100-Hz frequency in Figure 3c), with a somewhat bimodal distribution in the amplitude plane. This high-frequency high-amplitude content may indicate high-intensity seismic activity with temporal amplitude variations.

The distances between station pairs C1 – C2, C2 – C3, and C3 – C4 were 3.2, 1.4, and 4.9 km, respectively. One may thus expect to observe a higher degree of agreement between the closest station pair C2 – C3 compared with the most spatially separated station pair C3 – C4 (Figure 1). However, this is not the case, which suggests that each station is shaped by the dynamics of its local environment at the kilometer scale and that some key differences may be produced by the debris mantle.

No significant differences in noise level among seismic components were found (see the supporting information for more details and the methodology; Lecomte et al., 2008; Nakamura, 2008; Picotti et al., 2017; Preiswerk et al., 2017; Yan et al., 2018).

3.2. Temporal Changes in Ambient Noise

All of the discussed time series are hereafter shown in local Nepal time for convenience (UTC+ 5 hr 45 min). Noise is compared with the hourly air temperature and wind speed measurements obtained at the AWS site. Temperature was also recorded at the mass balance stakes (T1 and T2) and on rock on the west side of the glacier between stations C3 and C4 (T3; Figure 1). These temperature measurements are provided in Figure S2, and they were highly correlated with the AWS records ($r = 0.88$; p value $< 10^{-80}$), with the main difference being in amplitude. It is worth noting that the temperature was above or near 0 during the daytime, with significant daily variations of up to 12 ° C and 18 ° C at the lowest and the highest sites, respectively (Figure S2).

The seismic response at a given station and the physical parameters that characterize the station location consist of considerably different measurements, thus making a direct comparison of the actual observations difficult. However, by determining the anomalies of the seismic and meteorological observations at each station (see details in the supporting information), a comparative analysis of these anomalies allows any time-dependent variations to be detected and also allows the degree of correlation between the observations to be readily obtained.

The wind speed appears to be in good agreement with air temperature (Figure S2b). This relationship between the valley wind speed and air temperature (Figure S2b) thus makes some of the interpretations challenging.

Examples of the temporal noise variations partitioned by a given frequency band are provided in Figure 4a for each station (see Figures S3 and S4 for a full version of all the observations). The most striking features of Figure 4a are the covariance of the diurnal temperature cycle and the amplitude of the seismic noise at all frequency bands above 1 Hz. Furthermore, a remarkable feature of this behavior is the ambient noise variation being in or out of phase with the temperature, which depends on station location and frequency band (Figure 4a). The anomalies of the full-length time series (shown in Figure S3) are cross-correlated to quantify this heterogeneous relationship, and the results are summarized as a matrix (Figures 4b and 4d). The

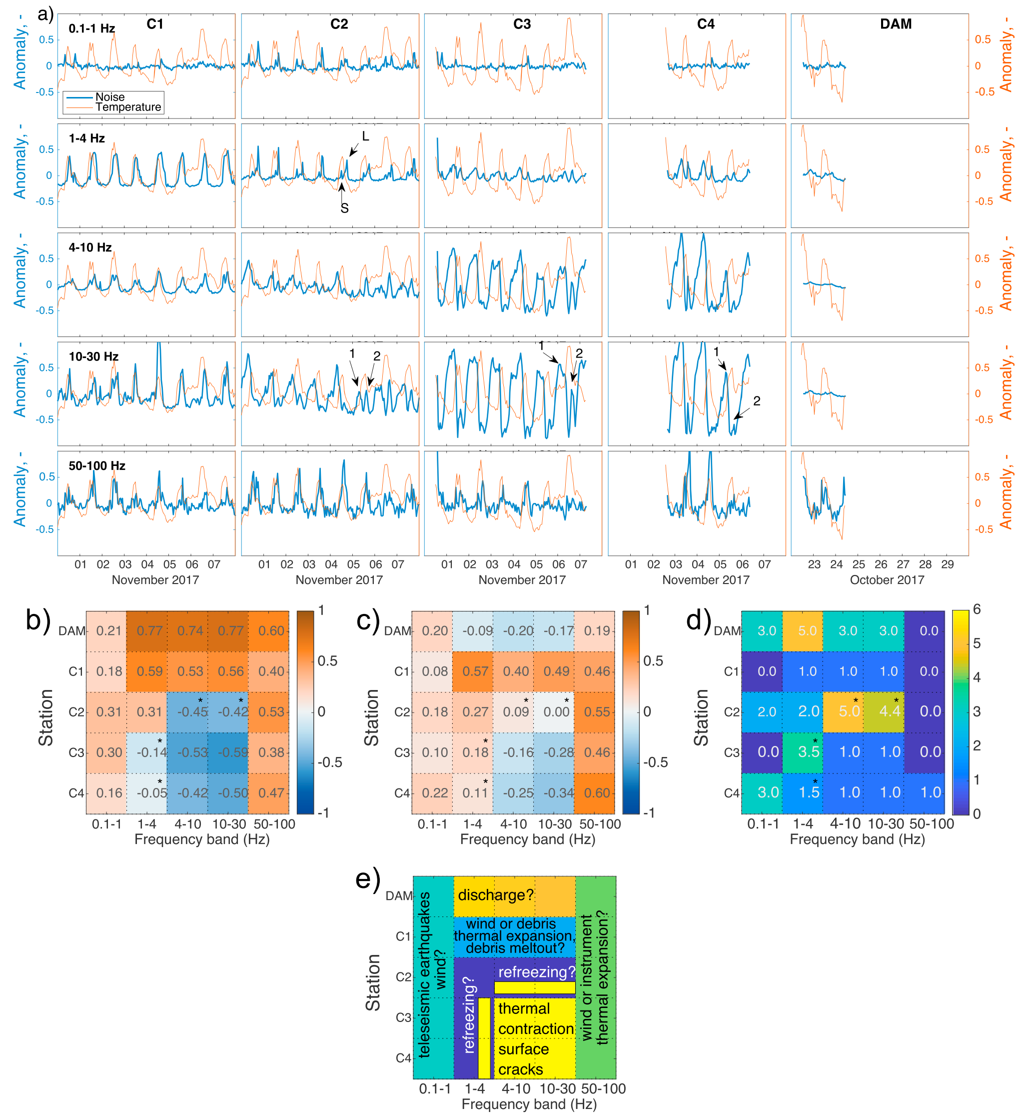

Figure 4. (a) Examples of the ambient noise anomaly variations at each station for the different frequency bands (blue), as well as the air temperature anomaly (T_{AWS}) variations (orange). The data from the four glacier stations (C1–C4) correspond to the same time interval, whereas DAM was in operation about a week earlier. Note that while the temperature data are the same for each station and time series, the temperature anomaly can vary between seismic stations, as it is dependent on the length of the time series at each station. (b, c) Cross-correlation results between the ambient noise and T_{AWS} (b) and (c) wind (U_{AWS}) anomalies, with (d) the corresponding lag of the noise anomaly behind the T_{AWS} anomaly. (e) Matrix of the major processes driving the observed ambient noise at each station. AWS = automatic weather station.

four correlation results marked with an asterisk (*; Figures 4b–4d) correspond to the time series with notable secondary peaks in noise amplitude, as detailed below. For the air temperature versus ambient noise comparisons, the time series were manually reevaluated, the lag between the main peaks was identified, and the corresponding cross-correlation coefficient values were assigned. Finally, the correlation coefficient is also computed at 0 lag for a comparison of the ambient noise with the wind anomalies (Figure S4), since it is reasonable to expect an instantaneous response, if any (Figure 4c).

3.2.1. Long- and Short-Period Noise

No clear daily cyclic dynamics were observed in the lowest frequency band (0.1–1.0 Hz) at most of the stations, likely due to the large distance from the ocean and the low sensitivity of the sensors. The only possible exception could be station C2, which shows elevated low-frequency noise levels in the afternoon and remains quiet between 7 p.m. and 9 a.m. The most probable source of this amplified signal is the close proximity of

C2 to a steep 2-km-high mountain slope facing the valley wind in the afternoon. Otherwise, only body waves from teleseismic earthquakes are anticipated to perturb this frequency band (Anthony et al., 2015). The other frequency band with a similar response across all stations, including the station at the terminal moraine, is the highest frequency band (50–100 Hz). A positive and nearly instantaneous correlation with air temperature and wind is observed for all stations (Figures 4b and 4c), which highlights that a common surface source produces the high degree of similarity between these very different sites. Visual inspection of the time series shown in Figures S3 and S4 suggests that wind is the most likely source. However, the similar high correlation with air temperature also leaves thermal expansion (due to solar heating) of the instrumental setup or nearby rock slopes as alternative explanations for this seismic response.

3.2.2. Midperiod Noise

The remaining range of analyzed frequencies (between 1 and 30 Hz) displays the most complex and interesting patterns. The debris-free stations (C3 and C4) clearly show the same response: a negative correlation with air temperature in the three frequency bins considered (1–30 Hz; Figure 4b), with a lag of 1–3 hr (Figure 4d). The negative correlation is also observed with the wind speed anomaly (Figure 4c). However, this correlation is clearly noncausative, as high noise levels at low wind speeds make no physical sense, which points to this likely being a product of the close relationship between air temperature and wind speed. It is therefore suggested that the higher noise levels at night and early in the morning correspond to higher seismic activity and intensity due to ice fracturing induced by tensile thermal stress from the decrease in temperature and radiative cooling (Figure 2).

The following two reasons highlight that it is difficult to find a meaningful alternative interpretation (e.g., ice flow variations) for the thermal cracking during the night and early morning. (1) It has been known since the work of Sanderson (1978) that even gross strain rates typical to fast-moving ice streams (10^{-3} a^{-1}) have no significant impact on the thermal stresses, because the corresponding background stress will be at the order of a fraction of 1 bar. For a slow-moving mountain glacier (with an ice speed decreasing from 27 m/a at the upper part to 3 m/a near the terminus, with no diurnal variation in ice speed discovered so far), the effect of background strain rate is also insignificant because it is 2 orders of magnitude smaller than the thermal strain rates. (2) Moreover, strain-rate variation is not likely to be a relevant mechanism for the observed late-night/early-morning increase in seismicity, since the glacier cannot speed up late at night. A speed up is possible in the afternoon with a delay of hours after temperature peak but is highly unlikely to continue till sunrise.

Similar phenomena of icequake, snowquake, and firn-quake occurrence at low temperatures (or at the onset of winter) have been observed in Franz Josef Land (Nansen, 1897) and in Antarctica (Lough et al., 2015; Nishio, 1983; Sanderson, 1978). Cooling-induced cracking was also observed in experiments on rocks (Browning et al., 2016). However, to our knowledge, intense nocturnal thermal fracturing of glacier ice and its possible modulation by debris have neither been previously observed instrumentally at temperatures warmer than −20 °C nor anticipated by the models (Nishio, 1983; Sanderson, 1978).

Furthermore, the stations on the debris-covered glacier surface, C1 and C2, show a positive or mixed relationship with temperature (Figure 4a). Interestingly, the correlation between the broadband noise and wind speed is also positive at C1 (Figures S4 and 4c), which will be discussed later in this section.

The relationship between ambient noise and the temperature is nontrivial at C2, as hybrid features are observed, especially at frequencies between 4 and 30 Hz. Specifically, the initially negative correlation (i.e., elevated ambient noise levels at the coldest temperatures) becomes disassociated into a double-peak oscillation after 4 November 2017. The latter double-peak feature is especially evident in the 10- to 30-Hz band ("1" and "2" in Figure 4a), indicating that the daytime peak existed earlier but was weaker. Such secondary peaks emerge approximately 4 hr after the temperature peak, thus implying no correlation with wind, and correspond to a steep drop in temperature due to the disappearance of direct sunlight. The rate of temperature change was calculated as the time derivative of the temperature anomaly (dA_T/dt) shown in Figure S5 to highlight this feature. The main daily peak at C2, in the 1- to 4-Hz frequency band, occurs at a similar timing. A probable concurrent process during this transitional period is the rapid refreezing of meltwater and an associated volumetric expansion within the debris mantle and surficial cracks. Moreover, the amplification of the secondary peak ("1" and "2" in Figure 4a) could be the sudden appearance of snow cover, as there was a heavy snowfall on the afternoon of 4 November. Snow cover could play a dual role in the seismic response of ambient noise, as it may correspond to damping the main night peak (presumably via thermal insulation, thus leading to a reduction in ice fracture-related amplitudes), or it may contribute extra meltwater on top of the debris cover, which may percolate into the debris cover and refreeze as the temperature falls.

Closer inspection of the C3 observations (e.g., see the 10- to 30-Hz band in Figure 4a) suggests the existence of a minor secondary peak that strengthens after 4 November, probably due to intensified melt and consequent refreezing (e.g., 6 November). The C4 observations also seem to have a secondary peak, although this latter peak does not increase in amplitude. The time series may simply be too short, however, which makes general sense, given that station C4 was deployed on the glacier surface for the shortest amount of time and also experienced insignificant surface melt due to the much colder conditions, with dry snow conditions observed at the time of station retrieval.

Upon revisiting the C1 observations (which show a positive correlation with air temperature and wind at all frequency bands above 1 Hz and a greater thickness of debris mantle than C2), it is suggested that debris cover protects the ice from high-amplitude temperature oscillations and therefore inhibits the intense near-surface fracturing of the glacier ice at night. Moreover, this thick debris cover may also inhibit the secondary minor peaks due to refreezing.

The maximum afternoon noise levels at C1 lag the air temperature by about an hour (Figure 4d), which suggests that these noise observations are most likely related to the valley winds or surface warming. On the one hand, the correlation coefficients between the seismic noise anomalies and the wind speed or the air temperature in the 1- to 30-Hz frequency bands are nearly identical on average (0.48 for wind versus a slightly higher 0.56 for temperature), making the interpretation ambiguous. However, while there is a good agreement between seismic noise and wind speed in the highest frequency band (50 – 100 Hz) at all stations, the lack of this seismic signal at lower frequencies for DAM, C2, C3, and C4 makes C1 an outlier. Furthermore, the median wind speed was rather low (1.5 m/s), which implies a noncausative correlation between the C1 broadband signals and wind speed. Regardless, surface warming should not be dismissed but rather given thorough consideration, especially since it may correspond to two interesting and difficult-to-monitor processes, namely, the increased mobility of the debris mantle due to thermal expansion and melt and increased meltwater discharge (see Podolskiy & Walter, 2016, for a review of fluvial and glaciohydraulic tremors).

3.2.3. Glaciohydraulic or Debris-Related Tremor?

If subglacial discharge fed by basin-scale runoff was responsible for the observed increase in broadband noise between 1 and 30 Hz, then the corresponding afternoon peak should appear at all stations. A daytime intensification of surface melt was obvious at the debris-free area around C3 due to intense solar radiation. Moreover, this station and the lower station C2 were located about 700 – 800 m from a site where subglacial water was continuously emerging from the glacier snout as a turbulent waterfall (Figure 1c). Furthermore, the time lag between the temperature and runoff peaks should be larger than 1 hr due to the delay in the basin-scale hydraulic response (Irvine-Fynn et al., 2017). However, the records suggest that the strength of the seismic tremor responded almost instantaneously to the temperature change (Figure 4a). These two lines of evidence thus make glaciohydraulic tremor an unlikely interpretation. Only DAM station had a notable 5-hr lag in tremor strength (the 1- to 4-Hz frequency band) behind the air temperature (Figures 4a and 4d), possibly pointing to the late afternoon increase in discharge through the nearby open channel. Unfortunately, runoff data are not available due to a malfunction in the water gauge.

The thermomechanical response of the debris mantle may also be considered a potential mechanism. Strong solar radiation results in rapid warming of the surface of the debris mantle, leading to the thermal expansion of the rock debris and inter-rock-ice melt at locations with thin debris. The volumetric increase of many tightly packed debris particles should intensify the stresses at the contacts between the rocks. It is therefore proposed that the continuous release of increased stress via discrete episodes of contact unlocking, slip, and particle repacking, together with the rolling of loose, melted-out particles over a wide area, including the steep-sided moraines on the southwest and northeast sides (Figures 1a and b), may collectively populate the local seismic wavefield.

However, adopting such a framework means that the dynamics observed at C2 do not fit this interpretation well. As seen in th e 1- to 4-Hz frequency band of Figure 4a, this station does have a minor daily peak in noise that coincides with the highest temperature (marked with *S*), but, the larger, main peak (marked with *L*) occurs later in the afternoon, during a rapid drop in temperature (Figure S5). As discussed earlier, the latter feature also appears in the high-frequency bands (4 – 10 and 10 – 30 Hz). When considering these high-frequency bands, it is more important to note that while C1 had a positive correlation with temperature, C2 had a negative correlation. The reasons for this discrepancy are unclear. As a working hypothesis, it is proposed that local differences between the sites shape the ambient noise response, such as (i) the thin debris mantle around C2 and thicker debris mantle around C1; (ii) the relatively flat surface area around C2 and more rugged around C1; and finally, (iii) C2 was close to off-glacier rock slopes and debris-free areas, while C1 was adjacent to a loose moraine with a slope gradient equal to the angle of repose (Figure 1b).

4. Conclusions

Diurnal variations in glacier seismicity have previously been reported along fast-moving ocean-terminating glaciers, with the seismicity linked to tide-modulated strain (e.g., Podolskiy et al., 2016). A clear diurnal fluctuation in the frequency of icequakes was also observed in the Greenland Ice Sheet ablation zone that was correlated with increased meltwater in the evening, resulting in more intense hydrofracturing (Röösli et al., 2014). Here it is shown that the observed variations in the ambient seismic noise of a slow-moving, debris-covered mountain glacier are driven primary by large fluctuations in temperature. Furthermore, significant site-dependent differences (summarized in Figure 4e) are found in the dynamics of the ambient seismic noise observed across the glacier and leading to several new questions. For instance, at this stage an empirical graphic relation between the amplitude of seismic noise and debris cover thickness of Figure 3c should be seen with caution since it can depend on physical properties of ice and debris. Detailed thermomechanical modeling would be a logical next step to address the latter relation. The conceptual model, which explains the main presented phase differences between the air temperature and ambient seismic noise, can be summarized as follows. Daily variations in temperature and corresponding volumetric changes in the glacier are accommodated by granular debris material. Without such a buffer, clean ice or surfaces with a thin debris layer are subjected to large temperature fluctuations and therefore to thermal contraction, which induces tensile ice fractures. Interestingly, snow cover seems to play a similar protective role to that of the debris by insulating the underlying ice and reducing icequake activity. This implies that a longer duration of ice exposure should correspond to a larger number of fracture cycles, especially at the end of the ablation season. Moreover, while a thick debris mantle dampens seismic activity early in the morning, it amplifies the seismicity during the daytime, presumably via the intensified local mobility of granular materials. However, this latter suggestion needs to be verified, as wind may provide an alternate interpretation.

Crevasses and cracks are fundamentally important components of glacier mass balance (Colgan et al., 2016). For instance, they serve as meltwater pathways into the englacial plumbing system and therefore bring a tremendous amount of latent heat into the glacier. However, to our knowledge, no previous study has focused on the ice fracture mechanics of debris-covered or Himalayan glaciers, suggesting that very little is known of the influence of cracks on the thermomechanical state of ice in such systems. Our findings thus provide the first evidence of a protective role of the debris mantle, not only via the well-known thermal insulation and reduction of surface melt but also via the limited amount of mechanical damage to near-surface ice, which leads to slower degradation of the glacier. However, the cyclic damage of exposed Himalayan ice may promote the rapid evolution of a *weathering crust* (Cook et al., 2016) and thus facilitate melt. This possibility should be further explored, especially since there is currently no consensus on the reason why Himalayan glaciers are more sensitive to temperature change than glaciers in other climates (Sakai & Fujita, 2017).

Acknowledgments
We sincerely thank F. Walter and M. Funk for the loan of the seismic instruments from the VAW/ETH Zürich instrument pool, H. Inoue and Y. Sato for support in the field and UAV images, H. Inoue and F. Walter for suggesting improvements to the manuscript, and "Guide For All Seasons" for logistical support. This study was supported by JSPS-KAKENHI grants 26257202 and 17H1621. The comments of two anonymous referees helped to improve the paper. The signal processing and figure production were done with the ObsPy, Pyrocko, and Matlab technical languages. The seismic and other presented data are available from Podolskiy et al. (2018).

References

Anthony, R. E., Aster, R. C., Wiens, D., Nyblade, A., Anandakrishnan, S., Huerta, A., et al. (2015). The seismic noise environment of Antarctica. *Seismological Research Letters*, *86*, 89–100. https://doi.org/10.1785/0220140109

Browning, J., Meredith, P., & Gudmundsson, A. (2016). Cooling-dominated cracking in thermally stressed volcanic rocks. *Geophysical Research Letters*, *43*, 8417–8425. https://doi.org/10.1002/2016GL070532

Chikita, K., Jha, J., & Yamada, T. (1999). Hydrodynamics of a supraglacial lake and its effect on the basin expansion: Tsho Rolpa, Rolwaling Valley, Nepal Himalaya. *AAAR*, *31*(1), 58–70. https://doi.org/10.2307/1552623

Chikita, K., Yamada, T., Sakai, A., & Ghimire, R. P. (1997). Hydrodynamic effects on the basin expansion of Tsho Rolpa Glacier Lake in the Nepal Himalaya. *Bulletin of Glacier Research*, *15*, 59–69.

Colgan, W., Rajaram, H., Abdalati, W., McCutchan, C., Mottram, R., Moussavi, M. S., & Grigsby, S. (2016). Glacier crevasses: Observations, models, and mass balance implications. *Reviews of Geophysics*, *54*(1), 119–161. https://doi.org/10.1002/2015RG000504

Cook, J. M., Hodson, A. J., & Irvine-Fynn, T. D. L. (2016). Supraglacial weathering crust dynamics inferred from cryoconite hole hydrology. *Hydrological Processes*, *30*(3), 433–446. https://doi.org/10.1002/hyp.10602

Ekström, G., Nettles, M., & Abers, G. A. (2003). Glacial earthquakes. *Science*, *302*(5645), 622–624. https://doi.org/10.1126/science.1088057

Fujita, K., & Sakai, A. (2014). Modelling runoff from a Himalayan debris-covered glacier. *HESS*, *18*(7), 2679–2694. https://doi.org/10.5194/hess-18-2679-2014

Fujita, K., Sakai, A., Takenaka, S., Nuimura, T., Surazakov, A., Sawagaki, T., & Yamanokuchi, T. (2013). Potential flood volume of Himalayan glacial lakes. *NHESS*, *13*(7), 1827–1839. https://doi.org/10.5194/nhess-13-1827-2013

Irvine-Fynn, T. D. L., Porter, P. R., Rowan, A. V., Quincey, D. J., Gibson, M. J., Bridge, J. W., et al. (2017). Supraglacial ponds regulate runoff from Himalayan debris-covered glaciers. *Geophysical Research Letters*, *44*, 11,894–11,904. https://doi.org/10.1002/2017GL075398

Kargel, J. S., Leonard, G. J., Shugar, D. H., Haritashya, U. K., Bevington, A., Fielding, E. J., et al. (2016). Geomorphic and geologic controls of geohazards induced by Nepal's 2015 Gorkha earthquake. *Science*, *351*(6269). https://doi.org/10.1126/science.aac8353

King, O., Quincey, D. J., Carrivick, J. L., & Rowan, A. V. (2017). Spatial variability in mass loss of glaciers in the Everest region, central Himalayas, between 2000 and 2015. *Cryosphere*, *11*(1), 407–426. https://doi.org/10.5194/tc-11-407-2017

Köhler, A., Chapuis, A., Nuth, C., Kohler, J., & Weidle, C. (2012). Autonomous detection of calving-related seismicity at Kronebreen, Svalbard. *Cryosphere*, *6*(2), 393–406. https://doi.org/10.5194/tc-6-393-2012

Larose, E., Carrière, S., Voisin, C., Bottelin, P., Baillet, L., Guéguen, P., et al. (2015). Environmental seismology: What can we learn on earth surface processes with ambient noise? *Journal of Applied Geophysics*, *116*, 62–74. https://doi.org/10.1016/j.jappgeo.2015.02.001

Lecomte, I., Thollet, I., Juliussen, H., & Hamran, S.-E. (2008). Using geophysics on a terminal moraine damming a glacial lake: The Flatbre debris flow case, Western Norway. *Advances in Geosciences*, *14*, 301–307. https://doi.org/10.5194/adgeo-14-301-2008

Lough, A. C., Barcheck, C. G., Wiens, D. A., Nyblade, A., & Anandakrishnan, S. (2015). A previously unreported type of seismic source in the firn layer of the East Antarctic Ice Sheet. *Journal of Geophysical Research: Earth Surface*, *120*, 2237–2252. https://doi.org/10.1002/2015JF003658

McNamara, D. E., & Buland, R. P. (2004). Ambient noise levels in the continental United States. *BSSA*, *94*(4), 1517–1527. https://doi.org/10.1785/012003001

Nakamura, Y. (2008). On the H/V spectrum. In *14th World Conf. Earthq. Engin.*, pp. 1–10.

Nansen, F. (1897). *Farthest north, vol. II*. New York: Harper & Brothers Publishers.

Nishio, F. (1983). Thermally induced fractures and snowquakes of polar snow cover. *Memoirs of National Institute of Polar Research Series C*, *14*, 1–48.

Nuimura, T., Fujita, K., Yamaguchi, S., & Sharma, R. (2012). Elevation changes of glaciers revealed by multitemporal digital elevation models calibrated by GPS survey in the Khumbu region, Nepal Himalaya, 1992–2008. *Journal of Glaciology*, *58*(210), 648–656. https://doi.org/10.3189/2012JoG11J061

Nuimura, T., Sakai, A., Taniguchi, K., Nagai, H., Lamsal, D., Tsutaki, S., et al. (2015). The GAMDAM glacier inventory: A quality-controlled inventory of Asian glaciers. *Cryosphere*, *9*(3), 849–864. https://doi.org/10.5194/tc-9-849-2015

O'Neel, S., & Pfeffer, W. T. (2007). Source mechanics for monochromatic icequakes produced during iceberg calving at Columbia Glacier, AK. *Geophysical Research Letters*, *34*, L22502. https://doi.org/10.1029/2007GL031370

Ojha, S., Fujita, K., Sakai, A., Nagai, H., & Lamsal, D. (2017). Topographic controls on the debris-cover extent of glaciers in the Eastern Himalayas: Regional analysis using a novel high-resolution glacier inventory. *Quaternary International*, *455*, 82–92. https://doi.org/10.1016/j.quaint.2017.08.007

Picotti, S., Francese, R., Giorgi, M., Pettenati, F., & Carcione, J. M. (2017). Estimation of glacier thicknesses and basal properties using the horizontal-to-vertical component spectral ratio (HVSR) technique from passive seismic data. *Journal of Glaciology*, *63*(238), 229–248. https://doi.org/10.1017/jog.2016.135

Podolskiy, E. A., Fujita, K., Sunako, S., Tsushima, A., & Kayastha, R. (2018). Seismic and meteorological records from Trakarding-Trambau Glacier system, Nepal Himalaya (21 October to 9 November 2017). *Zenodo*. https://doi.org/10.5281/zenodo.1323475

Podolskiy, E. A., Sugiyama, S., Funk, M., Walter, F., Genco, R., Tsutaki, S., et al. (2016). Tide-modulated ice flow variations drive seismicity near the calving front of Bowdoin Glacier, Greenland. *Geophysical Research Letters*, *43*, 2036–2044. https://doi.org/10.1002/2016GL067743

Podolskiy, E. A., & Walter, F. (2016). Cryoseismology. *Reviews of Geophysics*, *54*(4), 708–758. https://doi.org/10.1002/2016RG000526

Pore, N. A. (1979). Automated wave forecasting for the Great Lakes. *Monthly Weather Review*, *107*(10), 1275–1286.

Preiswerk, L., Michel, C., Walter, F., & Donat, F. (2017). Analysis of surface waves from ambient vibrations on Alpine glaciers in Switzerland. In *AGU Fall Meeting*, New Orleans, USA, pp. C41D–1255.

Rana, B., Shrestha, A. B., Reynolds, J. M., Aryal, R., Pokhrel, A. P., & Budhathoki, K. P. (2000). Hazard assessment of the Tsho Rolpa Glacier Lake and ongoing remediation measures. *Journal of Nepal Geological Society*, *22*, 563–570.

Röösli, C., Walter, F., Husen, S., Andrews, L. C., Lüthi, M. P., Catania, G. A., & Kissling, E. (2014). Sustained seismic tremors and icequakes detected in the ablation zone of the Greenland ice sheet. *Journal of Glaciology*, *60*(221), 563–575. https://doi.org/10.3189/2014JoG13J210

Roux, P.-F., Marsan, D., Métaxian, J.-P., O'Brien, G., & Moreau, L. (2008). Microseismic activity within a serac zone in an alpine glacier (Glacier d'Argentiere, Mont Blanc, France). *Journal of Glaciology*, *54*(184), 157–168. https://doi.org/10.3189/002214308784409053

Sakai, A., Chikita, K., & Yamada, T. (2000). Expansion of a moraine-dammed glacial lake, Tsho Rolpa, in Rolwaling Himal, Nepal Himalaya. *Limnology and Oceanography*, *45*(6), 1401–1408. https://doi.org/10.4319/lo.2000.45.6.1401

Sakai, A., & Fujita, K. (2017). Contrasting glacier responses to recent climate change in high-mountain Asia. *Scientific Reports*, *7*(1), 13717. https://doi.org/10.1038/s41598-017-14256-5

Sakai, A., Nishimura, K., Kadota, T., & Takeuchi, N. (2009). Onset of calving at supraglacial lakes on debris-covered glaciers of the Nepal Himalaya. *Journal of Glaciology*, *55*(193), 909–917. https://doi.org/10.3189/002214309790152555

Sanderson, T. J. O. (1978). Thermal stresses near the surface of a glacier. *Journal of Glaciology*, *20*(83), 257–283. https://doi.org/10.3189/S0022143000013836

Shrestha, B. B., Nakagawa, H., Kawaike, K., Baba, Y., & Zhang, H. (2011). Assessment of glacial hazards in Rolwaling Valley of Nepal and numerical approach to predict glacial lake outburst flood. *Annuals Disaster Prevention Research Institute, Kyoto University*, *54*(B), 565–591.

Wiens, D. A., Anandakrishnan, S., Winberry, J. P., & King, M. A. (2008). Simultaneous teleseismic and geodetic observations of the stick-slip motion of an Antarctic ice stream. *Nature*, *453*(7196), 770–775. https://doi.org/10.1038/nature06990

Yamada, T. (1998). *Glacier Lake and its Outburst Flood in the Nepal Himalaya. Monograph No. 1, March 1998*. Japan. Soc. Snow Ice: Data Center for Glacier Research.

Yan, P., Li, Z., Li, F., Yang, Y., Hao, W., & Bao, F. (2018). Antarctic ice sheet thickness estimation using the horizontal-to-vertical spectral ratio method with single-station seismic ambient noise. *The Cryosphere*, *12*(2), 795–810. https:doi.org/10.5194/tc-12-795-2018

Supporting Information for "Nocturnal thermal fracturing of a Himalayan debris-covered glacier revealed by ambient seismic noise"

Evgeny A. Podolskiy,[1,2] Koji Fujita,[3] Sojiro Sunako,[3]
Akane Tsushima,[4] and Rijan B. Kayastha[5]

Contents of this file

1. Supplementary text (Sections 1–6)
2. Table S1
3. Figure S1
4. Figure S2
5. Figure S3
6. Figure S4
7. Figure S5

Introduction

This Supporting Information (SI) file provides: (i) a table with descriptions of the seismic stations (Table S1), (ii) the network descriptions and site-specific features of each mentioned seismic station, method details of statistical characterization of ambient noise, anomaly definition, as well as a description of differences in noise level among seismic components (Sections 1-6), and (iii) supplementary figures showing seismic component analysis (i.e., H versus V), meteorological records, as well as a comparison of the seismic noise anomaly with air temperature and wind anomalies for the full duration of the campaign (Figs. S1–S5).

1. Tsho Rolpha and the terminal moraine

The surface area of Tsho Rolpa has increased about seven-fold since 1958, primarily due to glacier terminus retreat (65–100 m yr^{-1}) and ice melt at the bottom of the lake (0.2–1.2 m yr^{-1}) [*Chikita et al.*, 1999; *Sakai et al.*, 2000; *Shrestha et al.*, 2011; *Fujita et al.*, 2013]. It has been suggested that such an expanding water surface may intensify calving due to thermal undercutting by wind-driven water currents, leading to continued glacier retreat [*Sakai et al.*, 2009].

A significant geoengineering effort has been undertaken over the past couple of decades to decrease the water level in the lake. The water level was lowered about 3 m by July 2000, and an open channel was constructed on the southern side of the terminal moraine to continuously drain the excess lake water [*Rana et al.*, 2000]. Meteorological and water discharge data are currently acquired at the moraine and continuously monitored by the Department of Hydrology and Meteorology (DHM) of Nepal. There was concern of potential structural damage to the terminal moraine following the Gorkha earthquake of April 2015 [*Kargel and others*, 2016], and the water gate was temporarily closed to identify any water seepage through the moraine, with no evidence to support any recent weakening of the moraine. However, the northwestern side of the moraine has some buried dead-ice in its core [*Rana et al.*, 2000], as evidenced by ground-penetrating radar (GPR) profiles and electrical resistivity measurements [*Rana et al.*, 2000], as well as the temporal dynamics of small islets of debris near the moraine, which are gradually shrinking due to the melting of their ice content [*Sakai et al.*, 2000]. This means that, despite geotechnical, experimental, and modeling efforts to reduce or evaluate the dam failure potential [*Rana et al.*, 2000; *Shrestha et al.*, 2011], the structural stability of the moraine is still highly questionable, and thus remains a major unknown in the assessment of the glacial lake outburst flood (GLOF) hazard of Tsho Rolpa. Furthermore, the huge potential flood volume from a GLOF event at Tsho Rolpa [*Fujita et al.*, 2013] highlights the pivotal importance of maintaining glaciological monitoring in this area.

2. Seismic and other observations

The fieldwork began at Tsho Rolpha (4520 m a.s.l.) and progressively expanded to higher elevations, up to the accumulation area (5860 m a.s.l.). The timing of this ascent (and subsequent decent) constrained both the duration and timing of the seismic monitoring (Table S1). Therefore, the earlier installations (C1 and C2) were in operation longer than those at higher elevations (C3 and C4). The station at the terminal moraine that dammed Tsho Rolpha ("DAM") was installed for the shortest time period, being deployed while the team was acclimatizing to the high elevation at the start of the campaign, with this station then retrieved and deployed at a higher elevation once the team began the fieldwork.

Each seismic station was located on the glaciers and placed in a 30–60 cm deep glacier ice or debris pit, with the sensor placed on an aluminum tripod and covered with a protective metal net and a high-albedo blanket. Three-component geophones (PE-6/B by SENSOR Nederland) with an eigen-frequency of 4.5 Hz and a flat response in the velocity range between 4.5 and 150 Hz, were connected to DATA-CUBE[3] seismic recorders (by Omnirecs), with sampling at 400 Hz. Three data loggers had external global positioning system (GPS) antennae and were powered by external 12V–18Ah batteries that were charged with solar panels; one recorder had an internal GPS antenna and was powered by two internal Duracell 1.5 V–15Ah batteries.

Two time-lapse cameras (Garmin VIRB XE with GPS-synced internal clocks) were installed to take images at 1-min intervals (Fig. 1). The first camera (Cam1) was set on

[1]Arctic Research Center, Hokkaido University, Sapporo, Japan.
[2]GI-CoRE, Hokkaido University, Sapporo, Japan.
[3]Graduate School of Environmental Studies, Nagoya University, Nagoya, Japan.
[4]Research Institute for Humanity and Nature, Kyoto, Japan.
[5]School of Science, Kathmandu University, Kathmandu, Nepal.

0094-8276/18/$5.00

a side moraine in front of the glacier terminus to capture ice calving events into the proglacial lake, and the second camera (Cam2) was mounted on debris cover at station C2 to take off-glacier snow-avalanching slope images. A third camera (Brinno TLC200) was colocated with the Cam1 to acquire glacier-front images every 4 hours. However, the high-rate cameras were only in operation for 1–2 days in total due to a failure of the power supply during the low nighttime temperatures.

Among the auxiliary geophysical observations, the precise locations of seismic instruments were retrieved via differential GPS measurements, and GPR measurements of the ice thickness were conducted near each seismic station, depending on the physical accessibility of each location.

3. Site-specific features

Given that each seismic station was deployed in a unique glaciological environment (Table S1), yielding unique seismic signals that can be immediately seen from raw seismic traces, as shown in Fig. 2 of the main text, a concise description of each station location is provided below. Unmanned aerial vehicle aerial photographs were successfully obtained at four of the five sites, and are shown in Fig. 1b–e.

- DAM

The seismic station was placed in the center of the terminal moraine, about 10 m from Tsho Rolpa, an ice-free proglacial lake. It is possible that the moraine material under the seismic station consists of some dead-ice [*Rana et al.*, 2000]. The distance between the station and the open channel was about 200 m (Fig. 1a). The annual average discharge rate from the lake is $3\,\mathrm{m^3\,s^{-1}}$ [*Shrestha et al.*, 2011]. However, this rate is generally smaller in the late October to early November timeframe, after the summer monsoon, with a discharge of about $2\,\mathrm{m^3\,s^{-1}}$ [*Fujita and Sakai*, 2014]. Runoff feeds Tsho Rolpha mainly through the melting of glacier ice and precipitation within its $76.5\,\mathrm{km^2}$ catchment area [*Fujita and Sakai*, 2014].

- C1

The station was located about 500 m upglacier of the glacier terminus (Fig. 1b). The surrounding debris-covered area is highly heterogeneous, with rugged topography, ice cliffs, supraglacial ponds, and a debris mantle with a significant thickness (e.g., 0.65 m). Valley winds blow at 2–$7\,\mathrm{m\ s^{-1}}$ toward the glacier calving front between 10 AM and 7 PM local time (LT) on average [*Chikita et al.*, 1997]. However, the median 1-h-averaged wind speed measured at the AWS during the campaign was only $1.5\,\mathrm{m\ s^{-1}}$, with a peak speed of about $3\,\mathrm{m\ s^{-1}}$ that was usually observed around 12–2 PM LT; Fig. S2). These observed winds produce waves and surface currents that transfer heat toward the ice cliff [*Chikita et al.*, 1997]. Detailed studies of the Tsho Rolpa lake physics suggest the existence of sediment-laden flows near the lake bottom, generated by meltwater discharge presumably from a single subaqueous conduit with a diameter of about 10 m [*Chikita et al.*, 1997, 1999]. Rocks rolling down the side moraine walls were also occasionally heard in the area.

- C2

Station C2 had a thinner debris mantle than C1 on average (i.e., 0.23 m versus 0.65 m). Furthermore, the station (Fig. 1c) was located under the steep cliff face of Bigphera-Go Shar Mountain (6730 m a.s.l.). The slope of the mountain had many hanging glaciers, with ice and powder snow avalanches frequently triggered by collapsing seracs. The timing of any noted avalanche events was manually recorded while the field party was working and camping in the vicinity of sites C2 and C3.

- C3

Station C3 was located at the lowest part of the debris-free glacier surface, above a 500 m rock cliff (Fig. 1d), which had an active stream continuously flowing out from under the glacier terminus during the campaign despite the cold night temperatures. This area had surface melt in the afternoon due to the strong solar radiation and was completely frozen at night and in the early morning hours during the campaign. The snow avalanches mentioned in the C2 description, could also be seen and heard at site C3.

- C4

The highest-altitude station (5555 m a.s.l.) was set in the middle of the glacier, and no noticeable surface melt was observed during the campaign. However, there were a large number of longitudinal 10-m-deep canyons eroded into the glacier surface by meltwater during the monsoonal melt season (Fig. 1e). All surface ponds and streams were completely frozen during the campaign, and dry snow was covering the station upon retrieval.

4. Statistical characterization of ambient noise (PSD–PDFs)

The PDFs for our analysis were computed as follows. The continuous vertical-component seismic trace of each station is first divided into a series of 360-s segments, with a 50% overlap between consecutive segments. The PSD of each segment was then estimated after removing the instrument response and differentiating the velocity into acceleration over the 0.1–200 Hz range. The PSDs were smoothed in half-octave averages at 1/8-octave intervals. The powers of each times series were then collected in 0.5-dB bins, which were used for the statistical analysis of each frequency spectrum to produce the PDFs. Direct comparisons of the PSDs to the standard Global Seismographic Network noise models were made, with the PSDs presented in decibels (dB) with respect to acceleration ($\mathrm{m^2\,s^{-4}\,Hz^{-1}}$). Finally, for our analysis of PSDs integrated by frequency band, we worked with instrument-corrected relative displacements.

5. Anomalies

By determining the anomalies of the seismic and meteorological observations at each station, a comparative analysis of these anomalies is performed to determine the physical sources that shape the seismic response over time. The anomaly of a given time series is defined as the normalized deviations from a normalized mean, $A_{S,T,U} = X_{S,T,U} \pm |mean(X_{S,T,U})|$, with "+" for $mean(X_{S,T,U}) < 0$, and "–" for $mean(X_{S,T,U}) \geq 0$, where X is the observed time series, which may be either the seismic response of the station, $X_S = log_{10}(\frac{S(t)}{max|S(t)|})$, air temperature or wind speed, $X_{T,U} = \frac{V(t)}{max(|V(t)|)}$. Here the mean observation, $\hat{X}$, is unique to the specific time series of the seismic observations at a given seismic station, because each of the seismic stations was operational for a different length of time (2–14 days). Analysis of the anomalies (Figs. S2–S5) thus allows any time-dependent variations to be detected (e.g., diurnal), and also allows the degree of correlation between the observations to be readily obtained.

In the main text, it was noted that the wind speed appeared to be in good agreement with air temperature (Fig. S2b). Cross-correlation of the corresponding anomalies yields a 1-h lag of wind behind temperature (Fig. S2c). However, the improvement in the correlation coefficient (0.43; p-value $< 10^{-20}$) is negligible when compared with a direct Pearson correlation coefficient of 0.4 (i.e., at a 0-hour lag; p-value $< 10^{-17}$).

It could be argued that temporal variability of the wind speed measured at the AWS site was not representative for the entire study area. Station C1 was only 600 m from the AWS site; while stations C2 and C3 were 3.6 and 4.5 km further up the valley that has steep mountains on either side (almost in a direct line of sight). For a deep mountain valley it is very common to observe an increase in valley wind during the afternoon followed by a decrease at night. To assume that such configuration (and small scale) allow a significant difference in wind phase is unreasonable. Perhaps, some difference could be possible at the most distant station C4 (about 10 km from AWS), due to a turn of the valley, however, this station exhibited seismic records very similar to C3.

Finally, it should be noted that the 30–50 Hz frequency band was not included in the anomaly analyses presented here, because there were no distinct spatial or temporal anomalies present within this frequency band compared to 50–100 Hz frequency band.

6. Differences in noise level among seismic components

To identify the noise level differences between the three seismic components, we computed the average of the median horizontal power (radial and transverse components) and subtracted the median vertical power to obtain the H–V difference. The result shows no significant discrepancy in H–V (Fig. S1a). Only the station placed directly on the terminal moraine, DAM, showed amplification of its horizontal noise at around 2 Hz that was 6 dB higher than the ice sites. *Anthony et al.* [2015] hypothesized that such amplification could be due to wind forcing on the exposed rock outcrop.

We also evaluated the H/V spectral ratio to explore the possibility of alternative interpretations, as commonly done in earthquake-engineering studies for estimating the fundamental resonance frequency of sediment layers, which corresponds to seismic amplification [*Nakamura*, 2008]. In an earthquake-engineering context, the vertical motion in a soft layer is smaller than the horizontal motion, whereas they are similar for a rigid layer [*Nakamura*, 2008]. The H/V ratios computed for the quietest 1 percentile of noise at all glacial sites were nearly 1 ($\pm$0.20), with no significant peaks (Fig. S1b).

It could be argued that the H/V spectral ratio at C2 has a peak of 2 at 4 Hz (Fig. S1b). If this is not an artefact, then this would be equivalent to an ice thickness of about 114$\pm$11 m according to $H = V_s/4f$ [*Nakamura*, 2008], where the S-wave velocity, V_s, is between 1700 and 1950 m s^{-1} [*Podolskiy and Walter*, 2016]. However, given the lack of a similar signal at any of the other on-ice seismic stations, there is insufficient evidence to relate such a peak to a structural property of the glacier ice [e.g., *Preiswerk et al.*, 2017; *Picotti et al.*, 2017; *Yan et al.*, 2018].

In contrast to the on-ice stations, the terminal moraine station showed the most heterogeneous broadband H/V ratio, with an obvious peak of almost 7 at around 2 Hz, which could be due to geometrical and structural complexity of the moraine (Fig. S1b), and could be further studied with Finite Element Method modeling. Otherwise, the corresponding effective seismic velocity, V_s, assuming H = 150 m and f = 2 Hz, is 1200 m s^{-1}. According to seismic refraction investigations by *Lecomte et al.* [2008] on a terminal moraine damming a glacial lake in Norway, the best-fit P-wave velocities varied between 500 and 2000 m s^{-1}, leading the authors to conclude that no ice velocities were observed. Our results indicate a higher corresponding velocity, if we assume a Poisson solid, such that V_p can be approximated as $V_s \times \sqrt{3}$, which equates to a mean velocity of about 2165 m s^{-1}). This result could simply indicate the high rigidity of the moraine material, or it could point to the presence of an ice-layer in the velocity profile. However, the validity of these two hypothesizes can only be verified via geophysical methods or drilling through the terminal moraine.

References

Anthony, R. E., R. C. Aster, D. Wiens, A. Nyblade, S. Anandakrishnan, A. Huerta, J. P. Winberry, T. Wilson, and C. Rowe (2015), The Seismic Noise Environment of Antarctica, *Seism. Res. Lett.*, *86*, 89–100, doi:10.1785/0220140109.

Chikita, K., T. Yamada, A. Sakai, and R. P. Ghimire (1997), Hydrodynamic effects on the basin expansion of Tsho Rolpa Glacier Lake in the Nepal Himalaya, *Bull. Glacier Res.*, *15*, 59–69.

Chikita, K., J. Jha, and T. Yamada (1999), Hydrodynamics of a supraglacial lake and its effect on the basin expansion: Tsho Rolpa, Rolwaling Valley, Nepal Himalaya, *AAAR*, *31*(1), 58–70, doi:10.2307/1552623.

Fujita, K., and A. Sakai (2014), Modelling runoff from a Himalayan debris-covered glacier, *HESS*, *18*(7), 2679–2694, doi:10.5194/hess-18-2679-2014.

Fujita, K., A. Sakai, S. Takenaka, T. Nuimura, A. Surazakov, T. Sawagaki, and T. Yamanokuchi (2013), Potential flood volume of Himalayan glacial lakes, *NHESS*, *13*(7), 1827–1839, doi:10.5194/nhess-13-1827-2013.

Kargel, J. S., et al. (2016), Geomorphic and geologic controls of geohazards induced by Nepal's 2015 Gorkha earthquake, *Science*, *351*(6269), doi:10.1126/science.aac8353.

Lecomte, I., I. Thollet, H. Juliussen, and S.-E. Hamran (2008), Using geophysics on a terminal moraine damming a glacial lake: the Flatbre debris flow case, Western Norway, *Ad. Geo.*, *14*, 301–307, doi:10.5194/adgeo-14-301-2008.

Nakamura, Y. (2008), On the H/V spectrum, in *14th World Conf. Earthq. Engin.*, pp. 1–10.

Picotti, S., R. Francese, M. Giorgi, F. Pettenati, and J. M. Carcione (2017), Estimation of glacier thicknesses and basal properties using the horizontal-to-vertical component spectral ratio (HVSR) technique from passive seismic data, *J. Glac.*, *63*(238), 229–248, doi:10.1017/jog.2016.135.

Podolskiy, E. A., and F. Walter (2016), Cryoseismology, *Rev. Geophys.*, *54*(4), 708–758, doi:10.1002/2016RG000526, 2016RG000526.

Preiswerk, L., C. Michel, F. Walter, and F. Donat (2017), Analysis of surface waves from ambient vibrations on Alpine glaciers in Switzerland, in *AGU Fall Meeting*, pp. C41D–1255, New Orleans, USA.

Rana, B., A. B. Shrestha, J. M. Reynolds, R. Aryal, A. P. Pokhrel, and K. P. Budhathoki (2000), Hazard assessment of the Tsho Rolpa Glacier Lake and ongoing remediation measures, *J. Nepal Geol. Soc.*, *22*, 563–570.

Sakai, A., K. Chikita, and T. Yamada (2000), Expansion of a moraine-dammed glacial lake, Tsho Rolpa, in Rolwaling Himal, Nepal Himalaya, *Limnol. Oceanogr.*, *45*(6), 1401–1408, doi:10.4319/lo.2000.45.6.1401.

Sakai, A., K. Nishimura, T. Kadota, and N. Takeuchi (2009), Onset of calving at supraglacial lakes on debris-covered glaciers of the Nepal Himalaya, *J. Glac.*, *55*(193), 909–917, doi:10.3189/002214309790152555.

Shrestha, B. B., H. Nakagawa, K. Kawaike, Y. Baba, and H. Zhang (2011), Assessment of glacial hazards in Rolwaling Valley of Nepal and numerical approach to predict glacial lake outburst flood, *Annals of Disas. Prev. Res. Inst., Kyoto Univ.*, *54*(B), 565–591.

Yan, P., Z. Li, F. Li, Y. Yang, W. Hao, and F. Bao (2018), Antarctic ice sheet thickness estimation using the horizontal-to-vertical spectral ratio method with single-station seismic ambient noise, *The Cryosphere*, *12*(2), 795–810, doi:10.5194/tc-12-795-2018.

Corresponding author: E. A. Podolskiy, Arctic Research Center, Hokkaido University, Kita-21 Nishi-11, Kita-ku, Sapporo, 001-0021, Japan (evgeniy.podolskiy@gmail.com)

Table S1. Seismic station descriptions.

Name	Description	Location and Elevation	Observation days (in 2017)	Note
“DAM”	on the terminal moraine, in a depression between rocks	27.87095° N, 86.46324° E, 4521 m	Oct 22-24	Located near a water gauge that is monitored by the Department of Hydrology and Meteorology of Nepal. Perfect geophone level at retrieval.
“C1”	on ice, pit in a debris cover (0.38 m deep)	27.84546° N, 86.49247° E, 4594 m	Oct 25 - Nov 8	Colocated with an air temperature sensor (T1). Almost no geophone level loss at retrieval.
“C2”	on ice, pit in a debris cover, between rocks (0.58 m deep)	27.82939° N, 86.52001° E, 4777 m	Oct 28 - Nov 8	Colocated with an air temperature sensor (T2), and a time-lapse camera Cam2. Perfect geophone level at retrieval.
“C3”	on ice, ice pit (0.35 m deep)	27.83593° N, 86.53248° E, 5288 m	Oct 31 - Nov 7	Air temperature sensor (T3) located between C3 and C4. Slight geophone level loss at retrieval.
“C4”	on ice, ice pit (0.31 m deep)	27.87962° N, 86.54207° E, 5555 m	Nov 2-6	(Same as above.)

Figure S1. (a) Difference between the median vertical power and averaged horizontal power (H–V). (b) H/V spectral ratio for the quietest 1 percentile of the PDFs. The dB signal was first converted to acceleration to compute this ratio.

Figure S2. (a) Hourly air temperature observations recorded across the Trakarding-Trambau Glacier system during the period of seismic observations. (b) Hourly air temperature and wind speed observations recorded by the AWS. (c) Cross-correlation of air temperature to the wind anomalies. The red circle denotes the maximal correlation (r = 0.43) resulting from a +1 hour lag in wind speed after air temperature.

Figure S3. Anomaly variation in tremor strength at each station for the different frequency bands compared with the anomaly variation in the air temperature, A_T, at the AWS site. See the text for a definition of the anomalies.

Figure S4. Anomaly variation in tremor strength at each station for the different frequency bands compared with the anomaly variation in wind speed, A_U, at the AWS site. See the text for a definition of the anomalies.

Figure S5. Anomaly variation in tremor strength at each station for the different frequency bands compared with the time derivative of the anomaly variation in the air temperature, dA_T/dt, at the AWS site. See the text for a definition of the anomalies.

Fig. S1

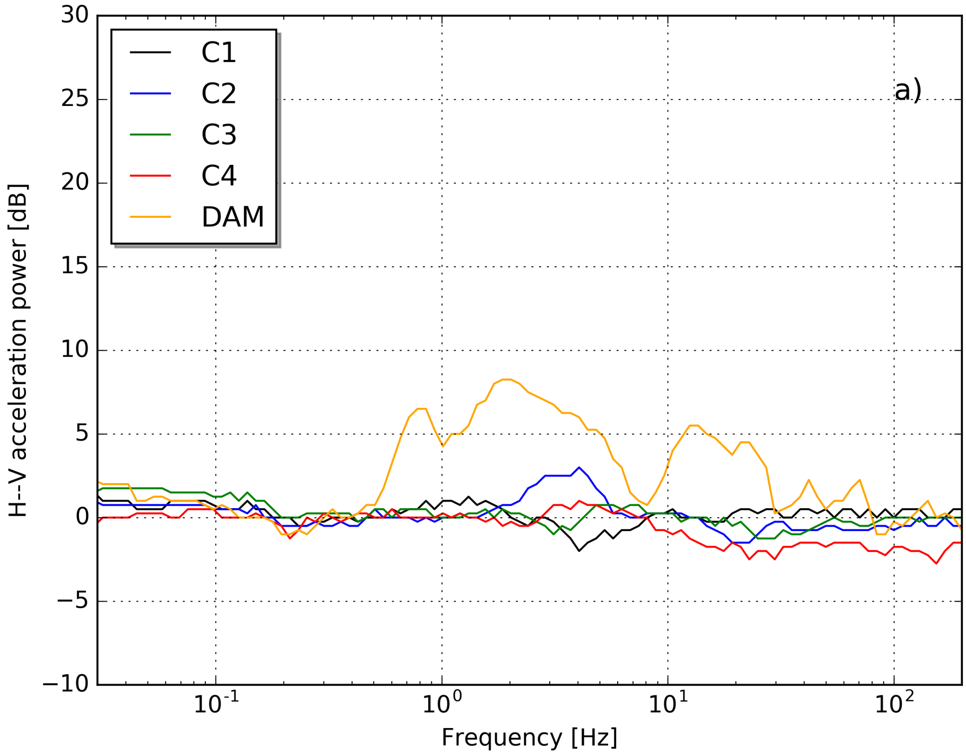
C1
C2
C3
C4
DAM
a)
H–V acceleration power [dB]
30
25
20
15
10
5
0
−5
−10
10^{-1}
10^{0}
10^{1}
10^{2}
Frequency [Hz]

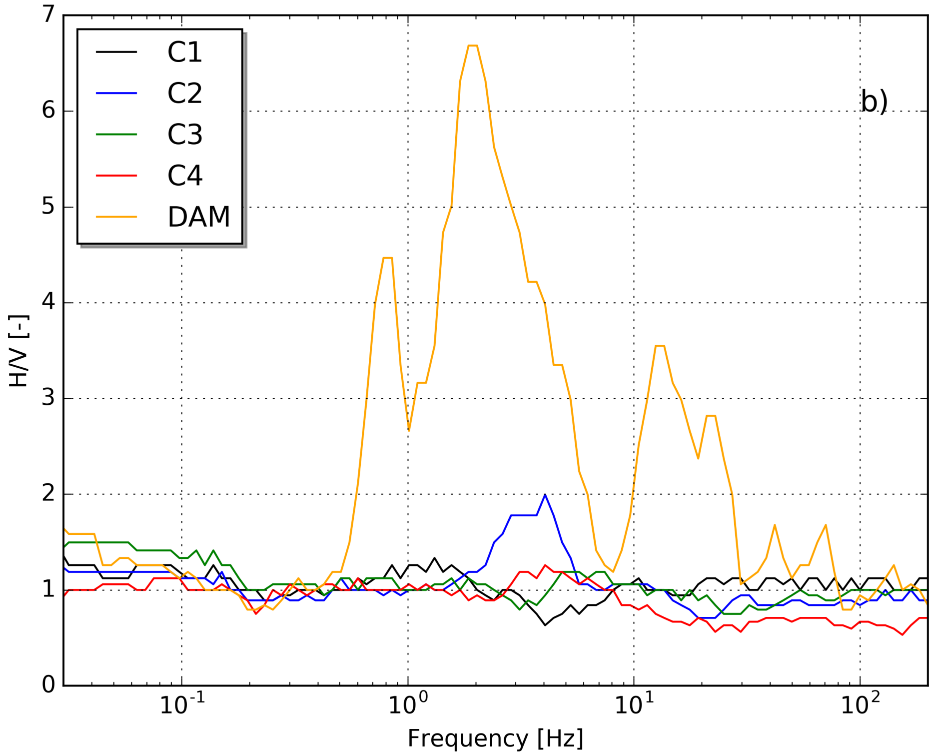
C1
C2
C3
C4
DAM
b)
H/V [-]
7
6
5
4
3
2
1
0
10^{-1}
10^{0}
10^{1}
10^{2}
Frequency [Hz]

Fig. S2

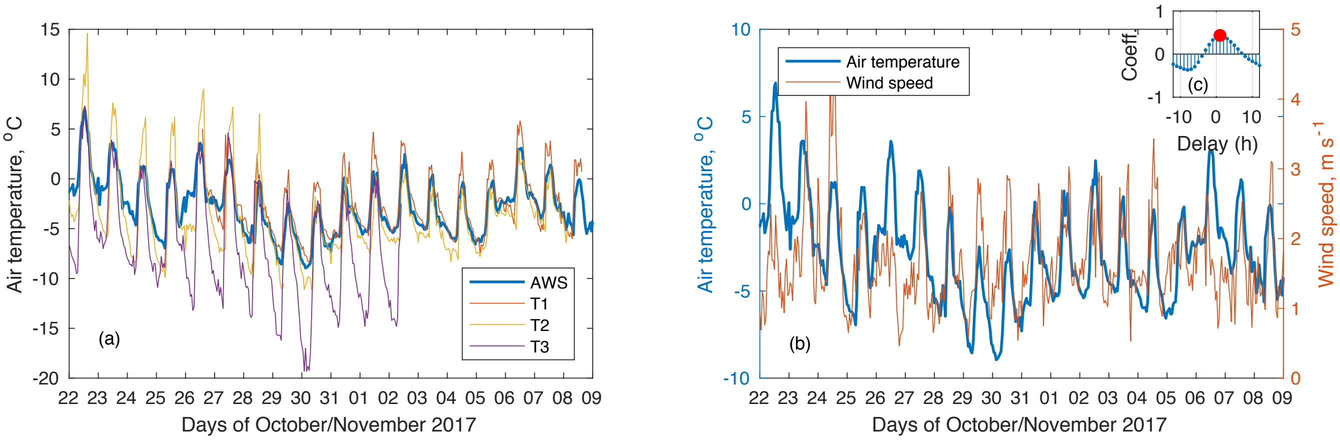

Air temperature, °C
AWS
T1
T2
T3
(a)
Days of October/November 2017
Air temperature
Wind speed
(b)
Wind speed, m s-1
Coeff.
(c)
Delay (h)

Fig. S3

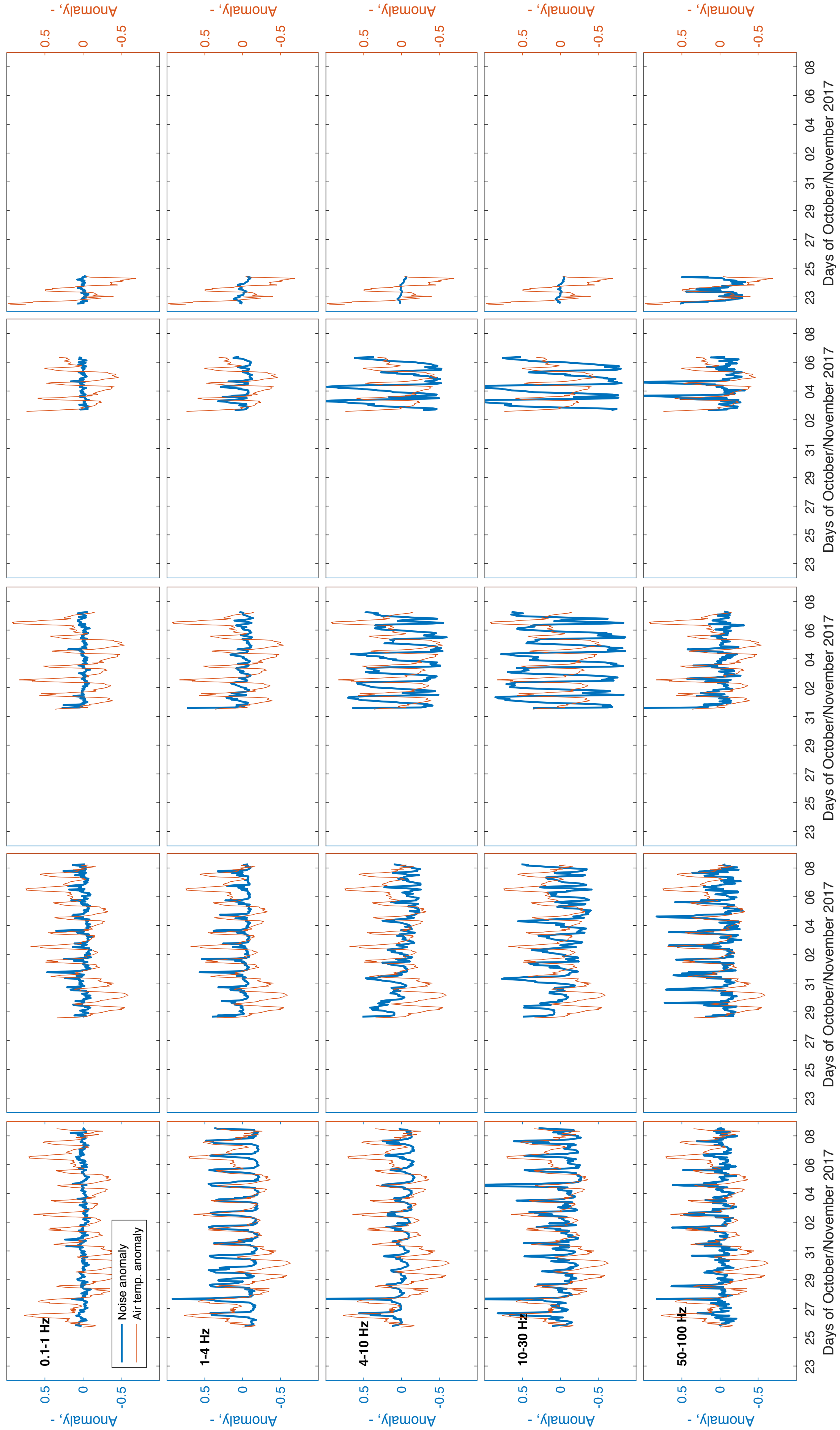
C1
C2
C3
C4
DAM
0.1-1 Hz
1-4 Hz
4-10 Hz
10-30 Hz
50-100 Hz
Noise anomaly
Air temp. anomaly
Anomaly, -
Days of October/November 2017

Fig. S4

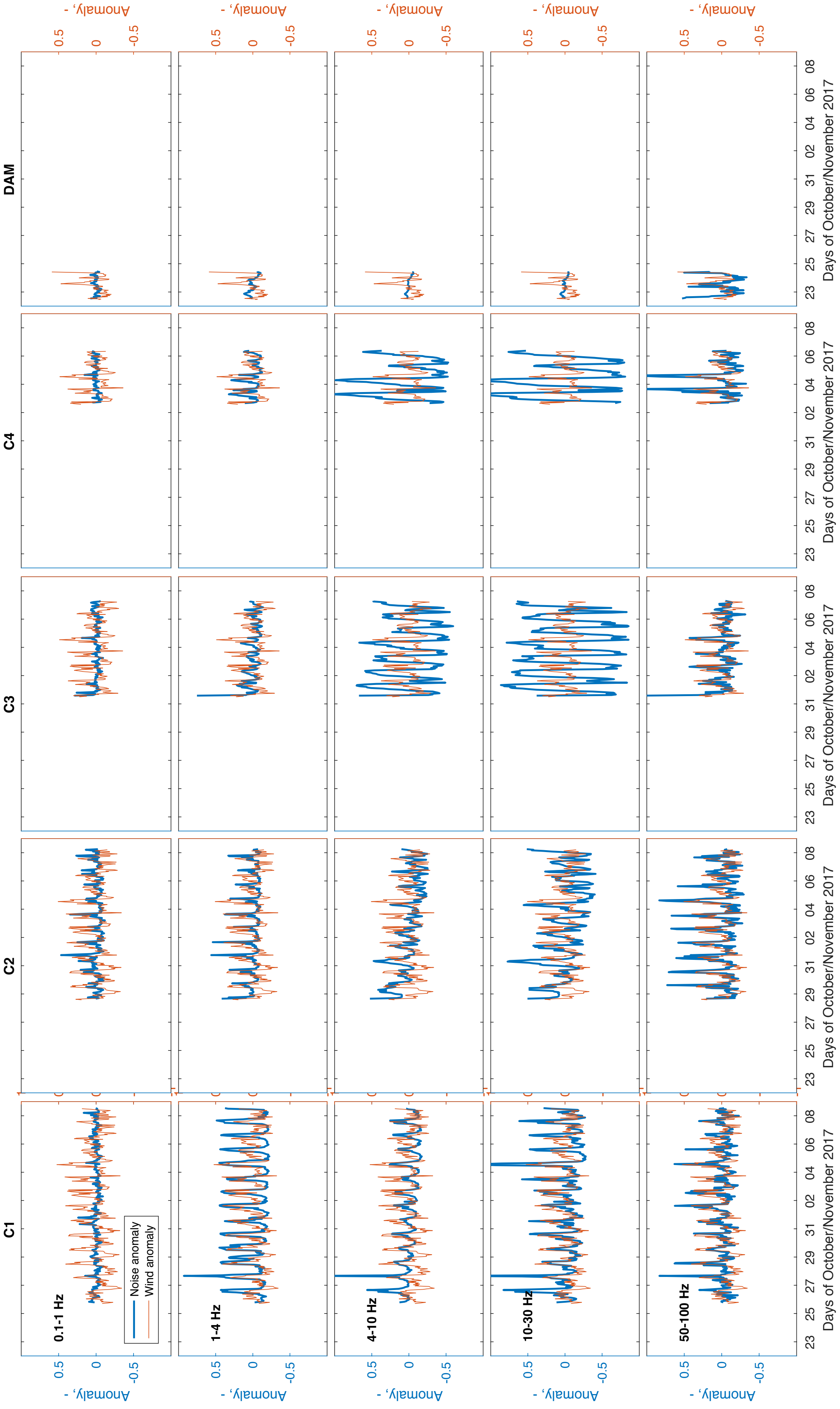
C1
C2
C3
C4
DAM
0.1-1 Hz
1-4 Hz
4-10 Hz
10-30 Hz
50-100 Hz
Noise anomaly
Wind anomaly
Anomaly, -
Days of October/November 2017
23 25 27 29 31 02 04 06 08

Fig. S5

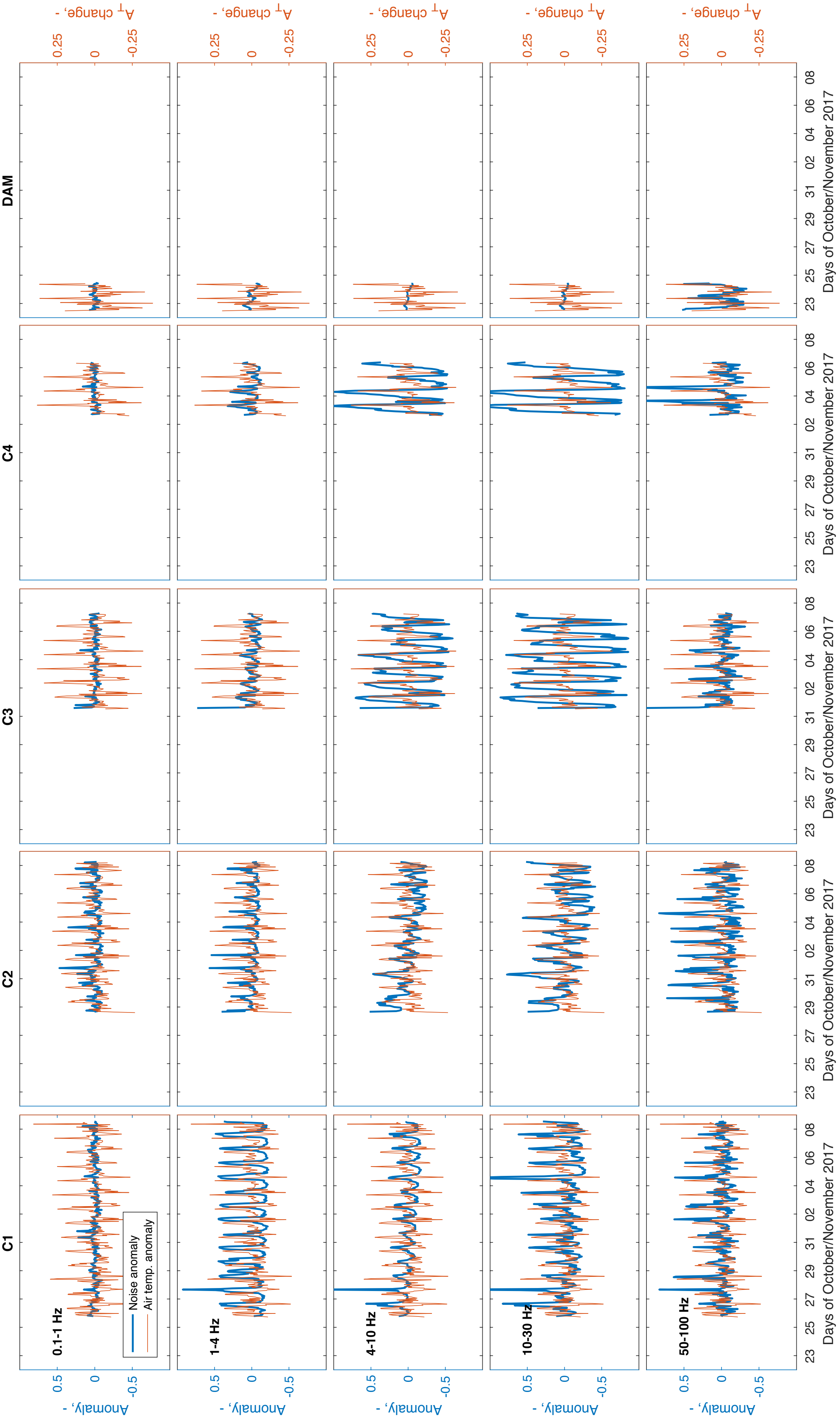

C1
C2
C3
C4
DAM
0.1-1 Hz
1-4 Hz
4-10 Hz
10-30 Hz
50-100 Hz
Noise anomaly
Air temp. anomaly
Anomaly, -
A_T change, -
0.5
0
-0.5
0.25
0
-0.25
23
25
27
29
31
02
04
06
08
Days of October/November 2017